Characterisation of signal enhancements achieved when utilizing a photon diode in deep Raman spectroscopy of tissue

Martha Z. Vardaki[1], Pavel Matousek[2,*] and Nicholas Stone[1,*]

[1]*School of Physics and Astronomy, College of Engineering, Mathematics and Physical Sciences, University of Exeter, Exeter EX4 4QL, UK*

[2]*Central Laser Facility, Research Complex at Harwell, STFC Rutherford Appleton Laboratory, Harwell Oxford, OX11 0QX, UK*

[*]*N.Stone@exeter.ac.uk*

[*]*Pavel.Matousek@stfc.ac.uk*

Abstract: We characterise the performance of a beam enhancing element ('photon diode') for use in deep Raman spectroscopy (DRS) of biological tissues. The optical component enhances the number of laser photons coupled into a tissue sample by returning escaping photons back into it at the illumination zone. The method is compatible with transmission Raman spectroscopy, a deep Raman spetroscopy concept, and its implementation leads to considerable enhancement of detected Raman photon rates. In the past, the enhancement concept was demonstrated with a variety of samples (pharmaceutical tablets, tissue, etc) but it was not systematically characterized with biological tissues. In this study, we investigate the enhancing properties of the photon diode in the transmission Raman geometry as a function of: a) the depth and b) the optical properties of tissue samples. Liquid tissue phantoms were employed to facilitate systematic variation of optical properties. These were chosen to mimic optical properties of human tissues, including breast and prostate. The obtained results evidence that a photon diode can enhance Raman signals of tissues by a maximum of ×2.4, although it can also decrease the signals created towards the back of samples that exhibit high scattering or absorption properties.

OCIS codes: (300.0300) Spectroscopy; (300.6450) Spectroscopy, Raman.

References and links

1. N. Stone, R. Baker, K. Rogers, A. W. Parker, and P. Matousek, "Subsurface probing of calcifications with spatially offset Raman spectroscopy (SORS): future possibilities for the diagnosis of breast cancer," Analyst **132**, 899-905 (2007).
2. P. Matousek and N. Stone, "Prospects for the diagnosis of breast cancer by noninvasive probing of calcifications using transmission Raman spectroscopy," J Biomed Opt **12**(2007).
3. P. Matousek and N. Stone, "Development of deep subsurface Raman spectroscopy for medical diagnosis and disease monitoring," Chemical Society reviews (2015).
4. N. Stone and P. Matousek, "Advanced transmission Raman spectroscopy: A promising tool for breast disease diagnosis," Cancer Res **68**, 4424-4430 (2008).
5. P. Matousek, "Raman signal enhancement in deep spectroscopy of turbid media," Appl Spectrosc **61**, 845-854 (2007).
6. K. Buckley and P. Matousek, "Recent advances in the application of transmission Raman spectroscopy to pharmaceutical analysis," J Pharmaceut Biomed **55**, 645-652 (2011).

7. J. A. Griffen, A. W. Owen, and P. Matousek, "Development of Transmission Raman Spectroscopy towards the in line, high throughput and non-destructive quantitative analysis of pharmaceutical solid oral dose," Analyst **140**, 107-112 (2015).
8. P. Matousek, "Enhancement of laser radiation coupled into turbid media by using a unidirectional mirror," J Opt Soc Am B **25**, 1223-1230 (2008).
9. C. Eliasson and P. Matousek, "Passive signal enhancement in spatially offset Raman spectroscopy," J Raman Spectrosc **39**, 633-637 (2008).
10. P. Matousek, N. Everall, D. Littlejohn, A. Nordon, and M. Bloomfield, "Dependence of Signal on Depth in Transmission Raman Spectroscopy," Appl Spectrosc **65**, 724-733 (2011).
11. M. J. Pelletier, "Sensitivity-Enhanced Transmission Raman Spectroscopy," Appl Spectrosc **67**, 829-840 (2013).
12. M. Z. Vardaki, B. Gardner, N. Stone, and P. Matousek, "Studying the distribution of deep Raman spectroscopy signals using liquid tissue phantoms with varying optical properties," Analyst **140**, 5112-5119 (2015).
13. B. W. Pogue and M. S. Patterson, "Review of tissue simulating phantoms for optical spectroscopy, imaging and dosimetry," J Biomed Opt **11**(2006).
14. I. E. I. Petterson, F. W. L. Esmonde-White, W. de Wilde, M. D. Morris, and F. Ariese, "Tissue phantoms to compare spatial and temporal offset modes of deep Raman spectroscopy," Analyst **140**, 2504-2512 (2015).
15. S. L. Jacques, "Optical properties of biological tissues: a review," Phys Med Biol **58**, R37-R61 (2013).
16. S. L. Jacques, "Skin Optics," in *Skin Optics*, (Oregon Medical Laser Center News, 1998).
17. I. V. Meglinski and S. J. Matcher, "Quantitative assessment of skin layers absorption and skin reflectance spectra simulation in the visible and near-infrared spectral regions," Physiol Meas **23**, 741-753 (2002).
18. T. D. O'Sullivan, A. E. Cerussi, D. J. Cuccia, and B. J. Tromberg, "Diffuse optical imaging using spatially and temporally modulated light," J Biomed Opt **17**(2012).
19. F. Bevilacqua, D. Piguet, P. Marquet, J. D. Gross, B. J. Tromberg, and C. Depeursinge, "In vivo local determination of tissue optical properties: applications to human brain," Appl Optics **38**, 4939-4950 (1999).
20. S. Fantini, S. A. Walker, M. A. Franceschini, M. Kaschke, P. M. Schlag, and K. T. Moesta, "Assessment of the size, position, and optical properties of breast tumors in vivo by noninvasive optical methods," Appl Optics **37**, 1982-1989 (1998).
21. A. Kienle and T. Glanzmann, "In vivo determination of the optical properties of muscle with time-resolved reflectance using a layered model," Phys Med Biol **44**, 2689-2702 (1999).
22. A. N. Bashkatov, E. A. Genina, V. I. Kochubey, and V. V. Tuchin, "Optical properties of human cranial bone in the spectral range from 800 to 2000 nm - art. no. 616310," Saratov Fall Meeting 2005: Optical Technologies in Biophysics and Medicine VII **6163**, 16310-16310 (2006).
23. C. T. Germer, A. Roggan, J. P. Ritz, C. Isbert, D. Albrecht, G. Muller, and H. J. Buhr, "Optical properties of native and coagulated human liver tissue and liver metastases in the near infrared range," Laser Surg Med **23**, 194-203 (1998).
24. J. L. Sandell and T. C. Zhu, "A review of in-vivo optical properties of human tissues and its impact on PDT," J Biophotonics **4**, 773-787 (2011).
25. M. J. C. Vangemert, R. Verdaasdonk, E. G. Stassen, G. A. C. M. Schets, G. H. M. Gijsbers, and J. J. Bonnier, "Optical-Properties of Human-Blood Vessel Wall and Plaque," Laser Surg Med **5**, 235-237 (1985).
26. A. N. Bashkatov, E. A. Genina, V. I. Kochubey, A. A. Gavrilova, S. V. Kapralov, V. A. Grishaev, and V. V. Tuchin, "Optical properties of human stomach mucosa in the spectral range from 400 to 2000 nm - art. no. 673401," International Conference on Lasers, Applications, and Technologies 2007: Laser Technologies for Medicine **6734**, 73401-73401 (2007).

27. Y. Pu, W. B. Wang, M. AL-Rubaiee, S. K. Gayen, and M. Xu, "Determination of Optical Coefficients and Fractal Dimensional Parameters of Cancerous and Normal Prostate Tissues," Appl Spectrosc **66**, 828-834 (2012).
28. T. Svensson, S. Andersson-Engels, M. Einarsdottir, and K. Svanberg, "In vivo optical characterization of human prostate tissue using near-infrared time-resolved spectroscopy," J Biomed Opt **12**(2007).
29. F. Sardanelli, F. Zandrino, A. Imperiale, E. Bonalde, M. G. Quartini, and N. Cogorno, "Breast biphasic compression versus standard monophasic compression in X-ray mammography," Radiology **217**, 576-580 (2000).
30. "Prostate Gland," in *The Great Soviet Encyclopedia*, I. The Gale Group, ed. (2010).
31. R. Michels, F. Foschum, and A. Kienle, "Optical properties of fat emulsions," Opt Express **16**, 5907-5925 (2008).
32. V. Ntziachristos, X. H. Ma, A. G. Yodh, and B. Chance, "Multichannel photon counting instrument for spatially resolved near infrared spectroscopy," Rev Sci Instrum **70**, 193-201 (1999).
33. T. O. McBride, "Spectroscopic Reconstructed Near Infrared Tomographic Imaging for Breast Cancer Diagnosis," (Dartmouth College, Hanover, New Hampshire, 2001).
34. J. S. Dam, C. B. Pedersen, T. Dalgaard, P. E. Fabricius, P. Aruna, and S. Andersson-Engels, "Fiber-optic probe for noninvasive real-time determination of tissue optical properties at multiple wavelengths," Appl Optics **40**, 1155-1164 (2001).
35. Y. L. Zhang, Y. Yin, X. H. Liu, Z. Q. Shi, L. Q. Feng, M. L. Liu, G. W. Zhu, Z. J. Gong, and B. Q. Qin, "Spatial-seasonal dynamics of chromophoric dissolved organic matter in Lake Taihu, a large eutrophic, shallow lake in China," Org Geochem **42**, 510-519 (2011).
36. P. Di Ninni, F. Martelli, and G. Zaccanti, "The use of India ink in tissue-simulating phantoms," Opt Express **18**, 26854-26865 (2010).
37. L. Spinelli, M. Botwicz, N. Zolek, M. Kacprzak, D. Milej, P. Sawosz, A. Liebert, U. Weigel, T. Durduran, F. Foschum, A. Kienle, F. Baribeau, S. Leclair, J. P. Bouchard, I. Noiseux, P. Gallant, O. Mermut, A. Farina, A. Pifferi, A. Torricelli, R. Cubeddu, H. C. Ho, M. Mazurenka, H. Wabnitz, K. Klauenberg, O. Bodnar, C. Elster, M. Benazech-Lavoue, Y. Berube-Lauziere, F. Lesage, D. Khoptyar, A. A. Subash, S. Andersson-Engels, P. Di Ninni, F. Martelli, and G. Zaccanti, "Determination of reference values for optical properties of liquid phantoms based on Intralipid and India ink," Biomed Opt Express **5**, 2037-2053 (2014).
38. P. H. Eilers and H. F. Boelens, "Baseline correction with asymmetric least squares smoothing," Leiden University Medical Centre Report (2005).
39. G. Y. Chen, S. E. Qian, and S. Gleason, "Denoising of hyperspectral imagery by combining PCA with block-matching 3-D filtering," Can J Remote Sens **37**, 590-595 (2011).
40. H. J. Butler, L. Ashton, B. Bird, G. Cinque, K. Curtis, J. Dorney, K. Esmonde-White, N. J. Fullwood, B. Gardner, P. L. Martin-Hirsch, M. J. Walsh, M. R. McAinsh, N. Stone, and F. L. Martin, "Using Raman spectroscopy to characterize biological materials," Nat. Protocols **11**, 664-687 (2016).

1. Introduction

Deep Raman spectroscopy (DRS), comprising principally of Spatially Offset Raman Spectroscopy (SORS) [1] and Transmission Raman Spectroscopy (TRS) [2], has been established in recent years as a promising tool for non-invasive disease diagnostics. The encompassing techniques can achieve a depth range of up to two orders of magnitude higher than conventional Raman spectroscopy [3], paving the way for novel medical diagnosis and other medical analytical applications *in vivo*.

Deep Raman techniques in turbid media are characterized by weak Raman signals due to diffuse scattering (and potentially absorption) of photons propagating through these samples.

This poses a particular challenge when it comes to recovering Raman signals from deeper layers in biological tissue. To improve Raman signal to noise ratios, traditional methods, such as the increase of laser power, collection time, improvement of collection efficiency etc., can be used [4]. Further improvements can be made by employing a signal enhancing element, a "photon diode", which was shown to provide a multifold enhancement of Raman signal in powder samples. This can be beneficial as an additional route to boosting accessible depths and sensitivity of deep Raman spectroscopy.

A photon diode comprises a dielectric bandpass filter which increases the collected Raman signal from a highly scattering sample when placed in close proximity to the sample surface centred on the laser illuminating zone. It acts, in essence, as an unidirectional mirror allowing photons of a given wavelength and angle of incidence (e.g. at normal incidence) to be transmitted through it on one side whilst the photons re-emitted from the diffusely scattering sample (a dominant loss mechanism in TRS of tissue and other diffusely scattering samples) to be reflected from it back into the sample due to the angular dependence of its reflectance properties [5]. In this way, the element prevents the loss of diffusely scattered photons which re-emerge from the sample at the point where the laser beam enters the sample, while it allows the collimated laser beam impacting on it at normal incidence to be transmitted through the filter from the other side.

The photon diode has been used in various deep Raman studies in the past, predominantly to achieve signal enhancement, mainly with pharmaceutical tablets. The photon diode enhancement of pharmaceutical tablets in a transmission mode is typically in the range of ×4-×10 of the mean volume signal when the tablet thickness varies between 3 and 7 mm [5-8]. The mechanism of enhancement has also been studied using Monte Carlo simulations yielding corresponding enhancement factors [5, 8]. A modified version of the photon diode element is also applicable in the SORS modality where it has been demonstrated for a 4.2 mm two-layer pharmaceutical tablet, exhibiting enhancement by a factor of ×4.5 for the front layer and ×2.2 for the back layer [9]. Further investigation of the enhanced Raman signal as a function of a layer depth has been conducted while probing a thin film of polymer into different depths of a 4 mm tablet, showing an overall enhancement of ×6 experimentally and ×4 using numerical models [10]. Alternative enhancement methods include hemispherical mirrors also returning emerging photons back into the sample at the illumination zone with reported enhancement factors of up to ×40 in 6.35 mm thick pharmaceutical tablets [11].

Studies exploring the dependence of Raman signal on the depth of its origin in biological samples have also been performed [12], but without the use of photon diode. Separate Raman measurements on biological tissue using a photon diode, reported an enhancement factor of ×1.6 for the mean volume signal of a 14 mm thick chicken breast [8] and ×1.5 for a high-Raman scatterer buried in a 2.7 mm depth of 27 mm porcine tissue [4], while both of the tissue samples were used to simulate a human breast.

The photon diode enhancement of Raman signals as a function of the depth of their origin is an aspect that has not been explored yet in biological tissue samples. Large differences between the optical properties of biological tissues and pharmaceutical tablets, such as the lack of absorption in tablets and the mean free scattering path length in tissues due to the difference in spatial scales does not allow us to assume identical behavior. In this paper, we explore the dependence of photon diode signal enhancement not only on the signal source depth but also on tissue optical properties using liquid tissue phantoms. The 30 mm thickness phantoms employed were of similar optical properties to various human tissues, and of similar dimensions to particularly breast and prostate. The tissue phantoms consisted of a scattering agent, an absorption agent and a high Raman cross-section compound located at a given depth representing, for example, a malignant element found in many cancerous conditions (e.g. calcifications). The purpose of this study was to characterise the enhancement effect of the photon diode as a function of the inclusion depth inside the phantom in a transmission mode and the optical properties of the tissue matrix (scattering and absorption coefficients).

2. Materials and methods

Tissue phantoms with inclusions and different optical properties are widely used to simulate tissues in optical spectroscopy and deep Raman techniques [13, 14]. The liquid phase of the phantoms allows high flexibility in the control of its optical properties.

In this study, Intralipid and Indian ink were used to induce scattering and absorbance, respectively, in the liquid tissue phantoms. Intralipid, a dilute mixture of emulsified fatty acids serves as a scattering medium whereas Indian ink, a dispersion of carbon particles, acts as a wide spectrum absorbing agent.

2.1 Tissue phantom optical properties

The phantoms were prepared to include most of the range of optical properties found in tissues. Because these values vary considerably and can overlap between different types of tissues, it was important to explore which of the different tissue types would benefit the most from the diode signal enhancement.

The optical properties of various tissues which we took into consideration are presented in Table 1 and their relative distribution and relation to the phantom properties in Fig. 1. The reduced scattering coefficients were calculated as a function of the excitation wavelength [15], whereas the absorption coefficients are based on literature values for skin [16], dermis [17], brain [18], white matter [19], breast [15, 20], fat [21], bone [22], liver [23]- at 850 nm, muscle [21], small bowel [24], aorta [25], stomach wall [26]. For prostate tissue both the reduced scattering and absorption coefficients were extracted from separate studies [27, 28].

Table 1: Optical properties of the different types of mammalian tissue as found in the literature. The reduced scattering coefficient values are presented in ascending order.

Tissue	**Reduced scattering coefficient (cm^{-1})** [15]	**Absorption coefficient (cm^{-1})**
Liver	6.58	0.6- 1 [23]
Prostate	4-9.5 [27, 28]	0.002- 0.7 [27, 28]
Aorta	7.07	3.16 [25]
Muscle	8.13	0.2- 0.3 [21]
Small bowel	8.80	0.05- 0.2 [24]
White matter brain	9.41	0.75- 1.15 [19]
Breast	9.84	0.068- 0.102 [20]
Brain (mean)	10.70	0.4 [18]
Stomach wall	11.68	2 [26]
Fat (mean)	13.09	0.02 [21]
Bone	15.93	0.2 [22]
Skin (mean)	22.39	0.25 [16]
Dermis	23.53	3 [17]

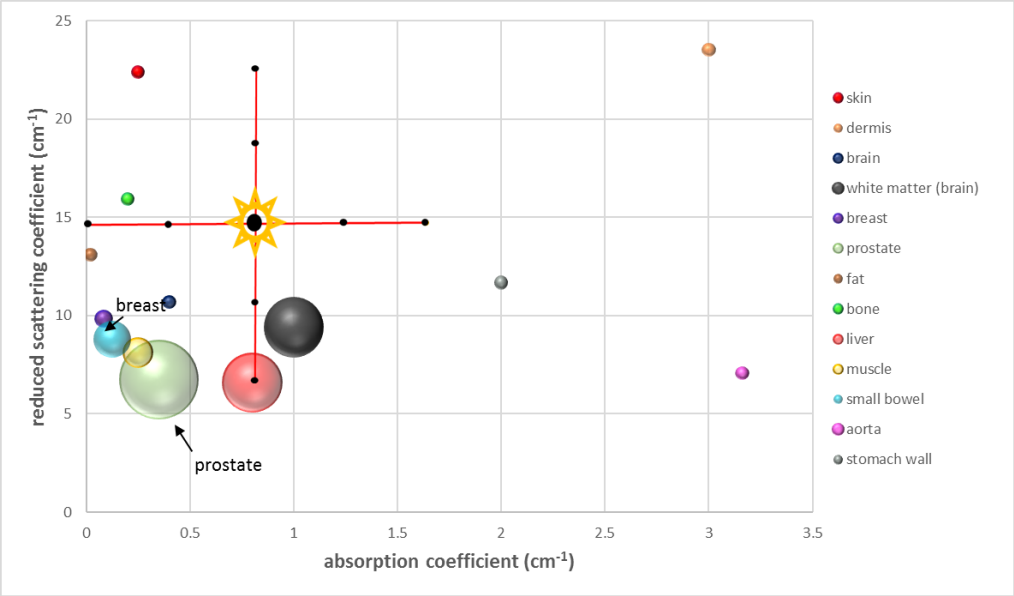

Fig. 1: Reduced scattering and absorption coefficient for different types of mammalian tissues obtained from literature data. Each sphere represents the range of optical properties for each individual type of tissue. The cross (shown with labels in Fig. 3) indicates the range of optical properties of the phantoms in the current study.

2.2 Tissue phantom preparation

The liquid tissue phantoms consisted of an optically clear quartz cell (45 mm width × 30 mm length (26 mm internal cell optical path length) × 45 mm height) (ramé-hart instrument co., USA) and contained aqueous solutions of Intralipid (20% emulsion, Sigma) and Indian ink (Histology Stain, American MasterTech), in various concentrations.

A thin vial (outer size: 12 mm width, 4 mm length; inner size: 10 mm width, 2 mm length in optical axis) filled with *trans*-stilbene and suspended from a motorized translation stage (8MTF-102LS05, Standa Ltd, Lithuania), was placed inside the quartz cell (Fig. 2). The vial width (12 mm) was aligned with the y-axis and the 4 mm length was aligned with the optical axis of the system (x-axis). Using the motorized stage, the *trans*-stilbene vial was moved to a number of different positions (depths) in a two-dimensional horizontal grid, inside the quartz cell during each mapping.

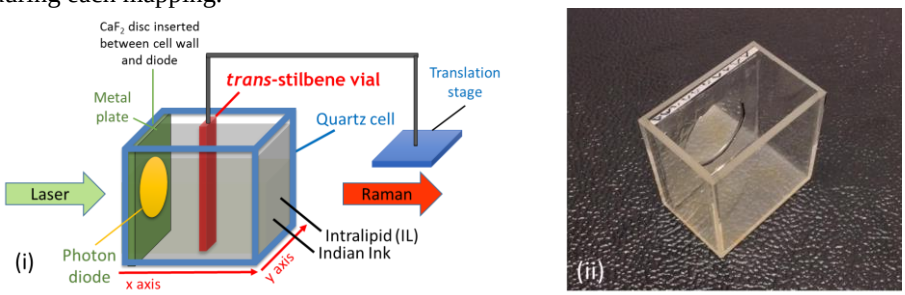

Fig. 2: (i) Liquid tissue phantoms components. (ii) Photon diode placed inside a metal plate and inserted inside the quartz cell in contact with the laser beam entrance wall when undertaking photon diode measurements.

As stated above the liquid tissue phantoms were designed to simulate human breast and prostate tissue (amongst others) both in size [29, 30] and optical properties. *Trans*-stilbene was selected for its high Raman cross-section and represents a localized region of abnormal tissue, e.g. a zone with micro-calcifications, which are often found in different types of cancerous tissues and have a distinctly different Raman signal from surrounding soft tissues (Intralipid and ink solution here). The purpose of the experiment was to study the effect of the photon diode on the Raman signal detected from the *trans*-stilbene vial at each location within the cell. The differences in Raman cross section between micro-calcifications and *trans*-stilbene are largely irrelevant in this study as the effect of the photon diode is linear in its nature and therefore the same enhancement factors would be achieved irrespectively of the magnitude of Raman scattering cross section of the material within the cell (other properties such as scattering and zero-absorption of *trans*-stilbene powder at the excitation and detection spectral ranges, were assumed to be approximately the same as for micro-calcifications).

In order to elucidate the role of both the absorption and scattering properties on the diode enhancement effect, the liquid tissue phantom studies were divided into two groups (Fig. 3):

a) Liquid tissue phantom measurements with a constant absorption coefficient (μ_a=0.8 cm^{-1}) and a varying reduced scattering coefficient (μ'_s=4.6-23.0 cm^{-1})

b) Liquid tissue phantom measurements with a constant reduced scattering coefficient (μ'_s=13.8 cm^{-1}) and a varying absorption coefficient (μ_a=0-1.63 cm^{-1})

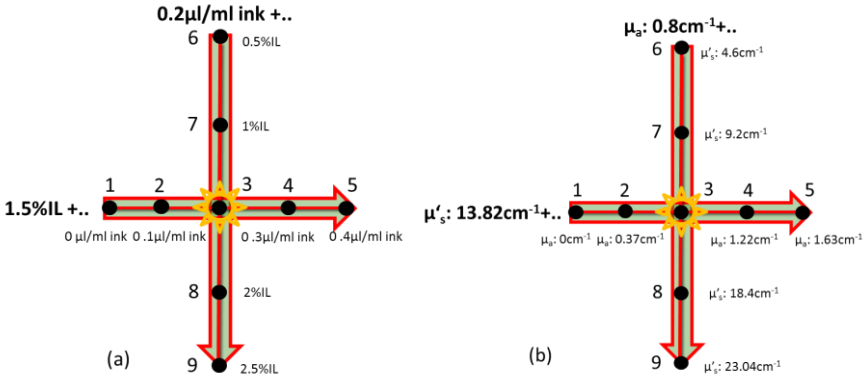

Fig. 3: Scatterer and absorber concentrations (a) and optical properties (b) of the liquid tissue phantoms prepared and measured with transmission Raman spectroscopy.

The liquid tissue phantoms were prepared and characterized in optical properties ranges similar to our previous study [12] in order to match a clinically relevant range. During the phantom fabrication, Intralipid was used as a scatterer and Indian ink as an absorber agent. Using literature values of reduced scattering coefficient for 10%, 20% and 30% of Intralipid [31] and extrapolating to values of lower concentration which agree with other studies[32-34] we calculated the Intralipid concentrations equivalent to the required reduced scattering coefficient values for our phantoms. For the Indian ink characterization, UV/Vis absorption spectra have been recorded for different ink concentrations and the values extracted for the appropriate wavelength (830 nm) to calculate the appropriate ink concentrations required for our phantoms [35]. It should be mentioned here that during the phantom characterization, Intralipid is assumed to have no absorption and Indian ink no scattering.

The optical properties of liquid tissue phantoms used are summarized in Table 2.

Table 2: Optical properties of the liquid tissue phantoms used in the study. The material used to provide the distinct Raman signal at given locations was *trans*-stilbene.

	μ'_s (cm^{-1})	μ_a (cm^{-1})

Phantom 1	13.82	0
Phantom 2	13.82	0.37
Phantom 3	13.82	0.8
Phantom 4	13.82	1.22
Phantom 5	13.82	1.63
Phantom 6	4.6	0.8
Phantom 7	9.2	0.8
Phantom 8	18.4	0.8
Phantom 9	23.04	0.8

It should be noted that during the study, the Intralipid absorption at 830 nm was checked before each experiment by recording UV/Vis measurements, for precipitation of lipid aggregates in order to ensure the preservation of its stability and consistency. Additionally, prior to sample preparation, the Indian ink was always subjected to ultrasound agitation in an ultrasonic bath for 30 minutes in order to prevent solution instability and ensure reproducibility of optical properties [36, 37].

2.3 Deep Raman Setup

We have used a deep Raman system at the University of Exeter arranged in a transmission Raman configuration. The setup is shown in Figure 4. It consisted of a spectrum stabilized laser (Innovative Photonics Solutions) with laser emission at 830 nm and an output power of ~300 mW. The laser light was coupled to a Thorlabs 400 μm multimode patch cord, collimated at exit and filtered by passing through a pair of laser line filters (FL830-10, Thorlabs) in order to suppress the amplified spontaneous emission (ASE) from the laser and other unwanted emission born in the optical fibre. The laser beam was directed towards the sample with a mirror and brought onto the sample with a 25 mm diameter, 70 mm focal length lens. The sample was illuminated with 280 mW of light in a 3–4 mm diameter spot. The collimated light passing through the tissue phantom is either scattered or absorbed by the sample components present. The Raman scattered photons were collected on the other side of phantom using a lens (f = 60 mm, dia. = 50 mm, AR coated, INGCRYS Laser systems). The collimated scattered light was passed through a holographic super notch filter (HSPF-830.0 AR-2.0, Kaiser Optical Systems) to remove the elastically scattered light (laser photons) and imaged onto a fibre probe bundle by a second lens of the identical parameters to the collection lens (i.e. no magnification was present). The fibre bundle (CeramOptec, 'spot to slit line' type bundle assembly, active area spot diameter approximately 2.2 mm, slit line of approximately 0.22 × 15.0 mm dimensions) was connected to the entrance port of a Holospec VPH system spectrograph (Kaiser Optical systems Inc, HSG-917.4 custom). The Raman spectra were recorded using a deep depletion CCD camera cooled down to −75 °C (Andor Technology, DU420A-BR-DD, 1024 × 255 pixels). The overall spectral resolution of the detection system was ~8 cm^{-1}.

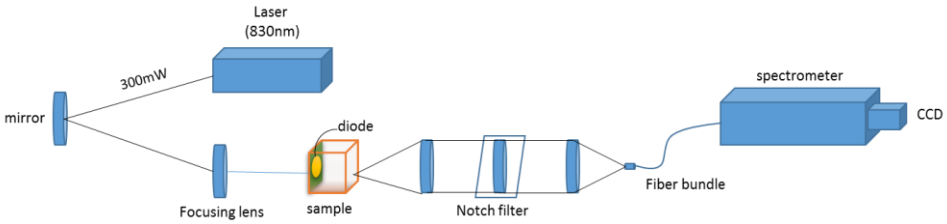

Fig. 4: Schematic diagram of the deep Raman setup in the transmission mode used.

In order to explore the properties of diode enhancement on Raman signal, a photon diode element (Semrock, 830 nm, with FWHM bandwidth measured as 9.5 nm, BrightLine® single-band bandpass filter – 25 mm diameter with overall 3.5 mm thickness) was mounted at the

center of a metal plate which was then placed at the front of the quartz cell against its internal wall (see Fig. 2). The metal plate outside the active area of the photon diode was covered with an aluminium reflecting foil, in order to achieve the maximum reflectance of re-emerging photons back to the phantom also outside the laser illumination zone. During the control (without a photon diode) measurements, a quartz window of identical dimensions was placed at the same location in order to make up for the loss of liquid phantom volume and to retain the identical mapping pattern. Additionally, a calcium fluoride disc (20 mm diameter, 1 mm thickness) was placed between the diode/quartz and the cell wall during every measurement, in order to minimize the solution volume trapped in the interface which would potentially lead to disruption of the collimated laser beam.

2.4 Raman mapping

In order to explore the diode enhancement effect on Raman signal through the different liquid tissue phantoms, we recorded the Raman spectra of the tissue phantom when the *trans*-stilbene vial was at 42 different positions on the optical axis of the setup. At each location the signal was collected using 6 accumulations of 5 seconds (30 s overall) and the cosmic ray removal option of the detector software (Andor Solis) was applied. The system was calibrated using Raman bands of an aspirin tablet (acetylsalicylic acid).

A motorized x-y translation stage was used to move the vial between different positions, in a 'snake'-like pattern (starting from the laser entrance side and moving towards the exit side of the cell). While recording the 1D maps, the step size on the x axis varied between 1 mm around the center of the phantom (between 8-14 mm from the illumination side) and 2 mm on the edges of the phantom (the rest of the mapping area). On the y axis only the main beam area (between 21-23 mm) was scanned, using 1 mm step size. At each step, a Raman spectrum was recorded and the stage was moved to the next position. In order to provide confidence in the results, each phantom was mapped three times at the same locations. The mean and the standard deviation were calculated and displayed as error bars in the plots.

For the 2D plot generated from the Phantom 3 map (Figure 5), the vial was positioned at 176 different locations inside the quartz cell within the x-y (horizontal) plane. To make most efficient use of the experimental time, the area of the y axis covered was between 12 and 32 mm distance from the top edge of the cell. On the y axis, the step size was 1 mm in the main beam area (between 18-28 mm) and 2 mm on the rest of the mapping area. On the x-axis the mapping was performed with a 2 mm step size for the full accessible length of the phantom (0-20 mm).

2.5 Data analysis

All data were loaded into Matlab R2013a (MathWorks), where they were subjected to baseline correction using asymmetric least squares smoothing [38] and principal component (PC) noise reduction. Principal component analysis, a statistical method which is more commonly used to reveal the spectral variance throughout a dataset, is also useful for minimizing the noise in a set of spectra by reconstructing it only from the significant principal components (in our case the first seven PCs). In this way, all of the important spectral information is retained, whereas the background noise is being removed [39, 40]. For the 1D plots, the mean intensity on the y axis was calculated in order to directly compare the values between the different maps.

Both one and two dimensional plots of the signal distributions are given. These plots display the trans-stilbene peak intensity, at each spatial location in the phantoms, at 1193 cm^{-1} for all the phantoms except for Phantom 1 (phantom with zero absorption), where 1594 cm^{-1} peak has been used instead, in order to avoid saturation issues.

3. Results

3.1 Effect of photon diode on the origin of Raman signal within the liquid phantoms

To evaluate the impact of the photon diode on the signal enhancement and the origin of Raman scattering, we first recorded a full map of Phantom 3 (μ'_s= 13.82 cm^{-1}, μ_a= 0.8 cm^{-1}) with and without the photon diode (Fig. 5). The color of the pixel indicates the peak intensity of 1193 cm^{-1} from *trans*-stilbene at each location.

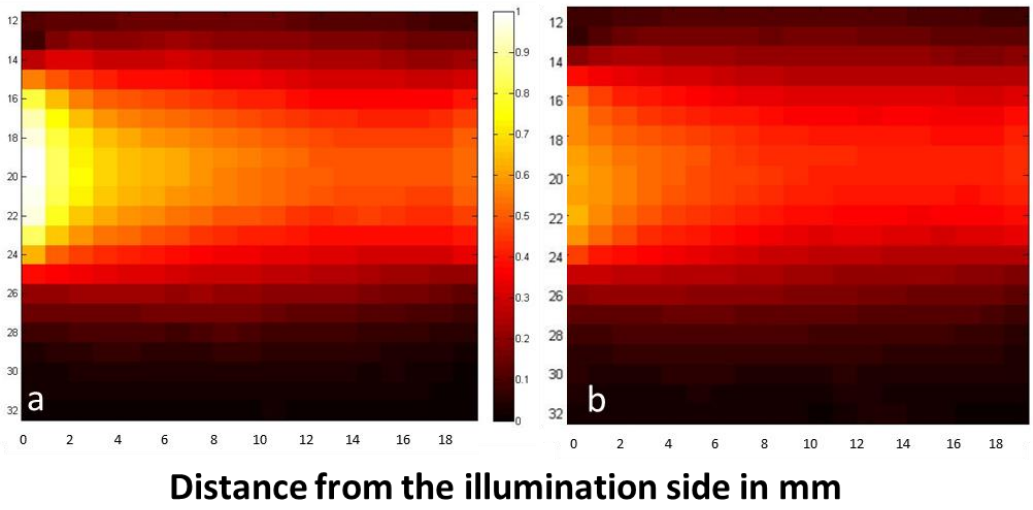

Fig. 5: Raman scattering 2D plots of Phantom 3 (μ'_s= 13.82 cm^{-1}, μ_a= 0.8 cm^{-1}) with (a) and without (b) the photon diode in a transmission mode. Laser photons are injected on the left of the image and Raman signal is collected on the right. The plots depict the intensity of ~1193 cm^{-1} Raman band of *trans*-stilbene as the vial moves to different positions in the phantom. The 2D plot (b) has been normalized against the maximum intensity of the diode map (a).

The photon diode provided an enhancement factor of ~×1.7 on the front of the phantom (closer to the illumination side) which decreased and remained stable in the middle of the phantom. This 2D plot is consistent with the results presented in the next part, where a variety of optical properties were explored.

3.2 Diode enhancement in phantoms with varying reduced scattering coefficient

The *trans*-stilbene generated Raman scattering has been recorded along the optical axis in phantoms with varying reduced scattering coefficient and a constant concentration of Indian ink.

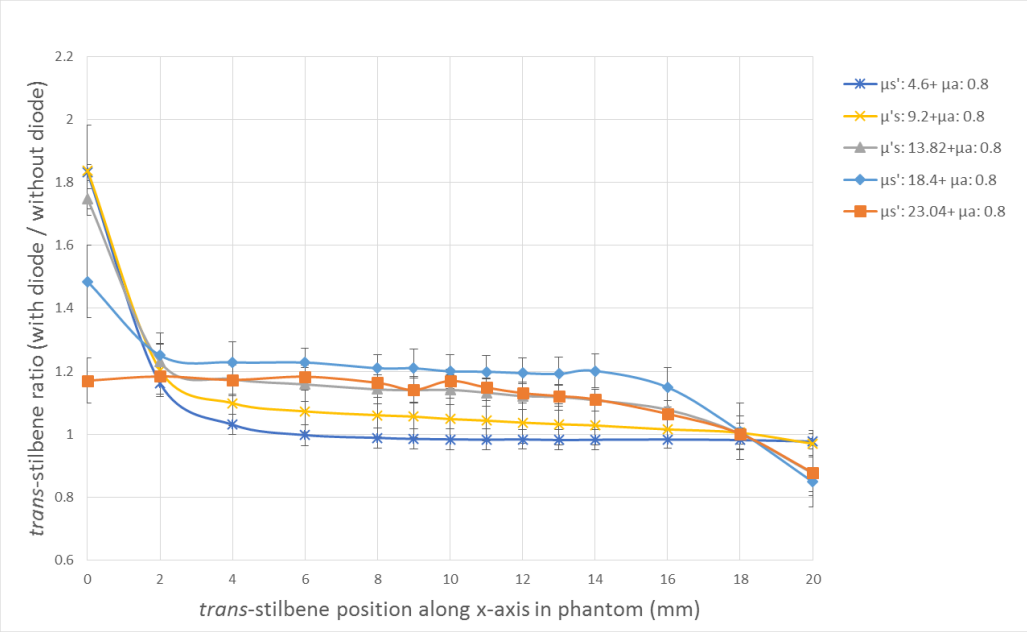

Fig. 6: Ratio of *trans*-stilbene Raman signal intensity with diode over signals without the diode versus the *trans*-stilbene vial position along the x-axis in the phantom (mm), for phantoms with the same absorption but different scattering coefficients. The coefficients are presented in cm^{-1}.

The reduced scattering coefficient values explored were in the range of 4.6 – 23.04 cm^{-1}. For clarity and brevity, the ratio of the *trans*-stilbene signal with the diode over the signal without the diode, was plotted against the phantom depth of the *trans*-stilbene vial, for phantoms with different optical properties, on the same plot (Fig. 6). The greatest enhancement factor for the phantoms with varying scattering, is observed on the measurement points with the closest proximity to the diode (0 mm). At this depth, phantoms with lower optical properties exhibit higher Raman signal with the diode, as the generated Raman photons cross the phantom bulk on the other side of the vial and are collected from the optics more efficiently in low scattering values. When the vial is positioned in a distance from the diode, the phantoms with the higher scattering benefit from the photon diode the most, with enhancement factors ranging between 1.17 and 1.83. The reason for that is that due to lower diffuse scattering, the low scattering phantoms do not benefit as much from the back-scattering enhancement mechanism of the diode. As a result, in a higher scattering environment, there is greater enhancement from the photon diode as the photons which re-enter the phantom volume reach the vial more easily due to diffuse scattering. In this way, the bulk volume of the phantom is the zone benefiting most from the presence of the photon diode. The signal enhancement decreases as we move towards (0-4 mm) and it seems to plateau when the *trans*-stilbene vial is located around the middle of the phantom (4-16 mm). The enhancement factors in this area appear to fall to a similar range (1.0-1.2) for most of the phantoms. Towards the back of the phantom and closer to the collection side (16-20 mm), the diode enhancement of the signal seems to be decreasing even more. This drop is in some cases so sharp (e.g. Phantom 8: μ_s'= 23.04 cm^{-1} and μ_a= 0.8 cm^{-1}), that the diode might not be beneficial for signal enhancement at all. It should be noted that at high scattering coefficient values (18.4 cm^{-1} and 23.04 cm^{-1}), the enhancement at the back of the phantom does not follow the same trend as at the front. The drop is most likely due to the overall lower transmittance of the diode compared to quartz layer (by around 10%).

3.3 Diode enhancement in phantoms with varying absorption coefficient

Similar trends are observed in phantoms with varying absorption coefficients and constant reduced scattering coeffcient (concentration of Intralipid) (Fig. 7). The signal enhancement from the diode here seems to be almost constant through many vial depths in each of the different phantoms. The absorption appears to affect the diode enhancement to a greater extent compared to the scattering case, since the enhancement ratio drops quicker when we increase the absorption coefficient (ink concentration) rather than the scattering coefficient. Comparing the two plots (Fig. 6 and Fig. 7), it seems that a middle value of absorption (μ_a= 0.8 cm^{-1}) inhibits the signal enhancement in the middle of the phantom more compared to a middle scatterer value (μ_s'= 13.82 cm^{-1}). This means that it is less likely for the 'enhanced' laser photons to generate a Raman photon which will get detected on the collection side in the presence of ink. On the other hand, when only Intralipid concentration is increased, the absorption increases indirectly due to the path length change too, but not to such an extent.

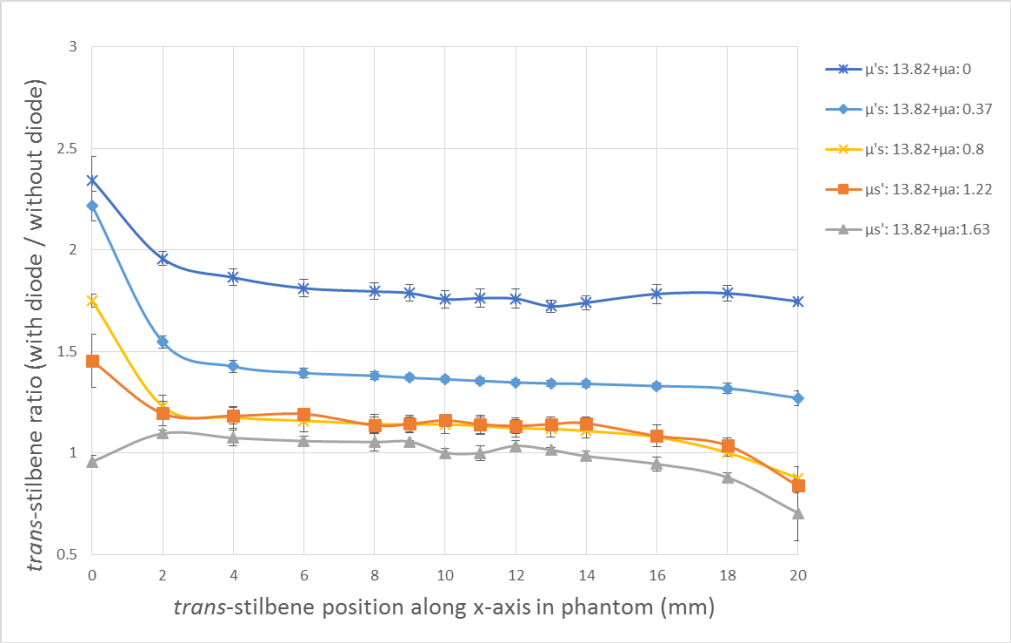

Fig. 7: Ratio of *trans*-stilbene signals with diode over signals without the diode versus the *trans*-stilbene vial position along the x-axis in the phantom (mm), for phantoms with same scattering but different absorption coefficients. The coefficients are presented in cm^{-1}.

In terms of the enhancement factor in the varying absorption phantoms, it takes a wide range of values through the entire phantom depth as the vial is moved across towards the collection side. The highest enhancement factor is again observed at the points closest to the diode (0 mm) and it takes different values between 0.95 and 2.34, depending on the absorber agent introduced in each phantom. As expected, the highest signal enhancement is observed in the phantom with no absorption and as soon as 0.1 μl/ml of ink is present, equivalent to μ_a of 0.37 cm^{-1}, the signal enhancement drops from 2.34 to 2.21. In the middle area of the phantom (4-16 mm), the signal enhancement has gradually decreased and reached a plateau. Towards the back of the phantom (16-20 mm), the signal enhancement seems to be decreasing even more and for the extreme ink concentration (Phantom 5: μ_a= 0.8 cm^{-1} and μ_s'= 13.82 cm^{-1}), the benefit of using a photon diode is limited, as the signal enhancement ratio constantly remains close or under 1. As mentioned before, the values below 1 can be attributed to the

reduced transmittance of photon diode which becomes especially significant in high optical properties phantoms with low signal to noise ratios.

It should be noted that a reduced signal on the edge of the sample is less detrimental to the detection sensitivity than it would be in the centre of the sample, as signals tend to be 10-50% higher at the edges than in the centre for tissue optical properties [12].

4. Conclusion

In this series of experiments, we have demonstrated the signal enhancement potential of photon diode in tissue phantoms with varying optical properties. It was shown that the gradual introduction of absorber agent affects the signal enhancement more strongly compared to a scatterer increase.

The enhancement factors observed through the measurements are in the range of 1-2.4. Similar studies on pharmaceutical tablets have exhibited an enhancement as high as ×10 [7]. However, the optical properties of these samples (e.g. lack of absorption) are quite different and their physical dimensions and those of illumination and collection zones are also different to those of biological tissues. To date, biological samples of similar thickness reported in the literature, show an enhancement of ~1.5 times for the entire sample matrix when measured in a transmission setup using a photon diode [4, 8]. These observations are in broad agreement with our results although these reports do not include any enhancement studies involving inclusions inside the phantoms. Our study also demonstrates how the diode enhancement changes with varying scattering and absorption properties in samples with Raman scattering.

Through our study, it is obvious that different tissue types will benefit to different extent from the use of photon diode. For example, based on the optical properties shown in Figure 1, tissues such as liver, prostate, breast, muscle, fat, brain, bone and small bowel would benefit with at least ×1.2 signal enhancement in the bulk volume, whereas other tissues such as dermis, white matter, skin and stomach wall would not see any benefit due to their higher optical absorption and scattering properties. In those tissues with regions of interest near the illumination side the photon diode may achieve signal enhancements of ×1.5 to ×2.3.

Where a signal enhancement is achieved it leads to enhanced detection sensitivity and penetration depth for transmission Raman measurements. Furthermore, the use of additional filters/mirrors on the remaining tissue/phantom sides (right, left, top, bottom and the collection sides) as indicated earlier [5] would provide the prospect for further improvements to Raman signal to noise ratios.

Acknowledgments

We thank the STFC BioMedical Network (STFC, STMA00012) and the University of Exeter for their financial support. An EPSRC grant [EP/K020374/1] partly funded the work presented here. We also thank Dr Ben Gardner (University of Exeter) for his support with data analysis.